MOF derived ZnO clusters on ultrathin Bi_2MoO_6 yolk@shell reactor: Establishing carrier transfer channel via PANI tandem S–scheme heterojunction

Aiwen Wang [a], Wei Wang [a], Jiaxin Ni [a], Dongqing Liu [a], Dongmei Liu [a,*], Jun Ma [a], Xuebin Jia [b,*]

[a] State Key Laboratory of Urban Water Resource and Environment (SKLUWRE), School of Environment, Harbin Institute of Technology, Harbin 150090, PR China
[b] School of Civil Engineering, Heilongjiang University, Harbin 150080, PR China

ARTICLE INFO

ABSTRACT

Solar driven semiconductor photocatalytic oxidation is a sustainable environmental remediation method. However, how to design an ideal interface for efficient photogenerated carrier transfer/separation is still the key to improve the photocatalytic performance. To solve this problem, we established a yolk@shell reactor by loading MOF derived ZnO clusters on ultrathin Bi_2MoO_6. The ZnO clusters can enhance the internal electric field and promote the directional migration of charge carriers to limit its recombination. More importantly, the high conductivity polymer PANI is coated to establish a high–speed electron transfer channel in tandem reactor, so that a large amount of carrier is accelerated to surface to participate in the oxidation reaction. The constructed heterojunction has great ability to degrade doxycycline under visible–light with a small amount of catalyst through the S–scheme transfer path. This work provides an important strategy for S–scheme heterojunction efficient carrier transfer and its application in environmental remediation.

1. Introduction

In recent years, the rapid development of industry and the growing global population are the key factors leading to energy shortage and environmental pollution. Therefore, the solar based advanced photocatalytic oxidation process, which uses low–cost semiconductor as catalyst, provides a more environmentally friendly and cost–effective strategy [1]. However, the separation and transport of photogenerated carriers to the surface is a prerequisite for redox reactions. Unfortunately, the biggest bottleneck encountered by photocatalysts is that serious carrier recombination (~ns) occurs during the transport process, which is the main culprit of low photocatalytic efficiency [2,3].

As a typical Aurivillius phase material in various Bi–based photocatalysts, Bi_2MoO_6 has been used for environmental remediation due to its moderate band gap, layered crystal structure and potential photocatalytic ability [4]. Moreover, it is well known that a single semiconductor photocatalyst cannot have both broad light absorption and sufficient redox capacity (Scheme 1a) [5]. The narrow band gap leads to rapid electron–hole recombination due to strong Coulomb attraction, and the driving force and rate constant of charge transfer are influenced by the Gibbs free energy variation [6]. Therefore, Bi_2MoO_6 (Eg is about

2.85 eV) can only absorb ultraviolet light and a small part of visible light, and the rapid recombination of charge carriers limits its quantum yield [7]. So far, many researchers have made many efforts to improve the photocatalytic efficiency of Bi_2MoO_6, such as ultrathin [8–10], hollow structure [11,12], oxygen vacancy [13,14] and special crystal surface exposure [15], etc. However, it is still challenging to develop a Bi_2MoO_6 catalyst with shorter distance electron transfer and enhanced redox capability under the premise of broad optical response. Fortunately, considering light utilization, redox capacity and charge recombination, the feasibility of constructing a suitable heterojunction system for the effective separation of electron–hole pairs have been demonstrated [16,17].

In the conventional type–II heterojunction, the photogenerated electrons will migrate from the reducing photocatalyst (RP) to the oxidation photocatalyst (OP), while the photogenerated holes will transfer in reverse, realizing their spatial separation (Scheme 1b). However, this charge–transfer path reduces the redox capacity, and Coulomb electrostatic repulsion between charge carriers will inhibit the transfer. Therefore, the conventional type–II heterojunctions has obvious limitations [18]. Recently, the concept of a S–scheme heterojunction was proposed by Yu's group [19], as shown in Scheme 1c.

When RP and OP are in contact, electrons in RP with higher Fermi energy levels will drift to the interface, leading to band bending. Thus, photogenerated electrons are transferred from CB of OP to VB of RP driven by Coulomb attraction, internal electric field and band bending under illumination. Conversely, electron transfer from CB of RP to CB of OP is also inhibited. Finally, strong photogenerated e^- and h^+ are transferred to VB of OP and CB of RP respectively, showing strong redox ability, while relatively weak carriers are recombined and eliminated [20]. However, the S–scheme heterojunction is still at the expense of weak photogenerated carriers. In recent years, many efforts have been made to improve the performance of S–scheme heterojunction, such as Au−assisted catalyst loading [21], 0D/2D interface regulation [22], inorganic/organic heterojunction construction [23], surface oxygen vacancy design [24], p − n type semiconductor regulation [25] and the introduction of quantum dots [26], etc. Nevertheless, how to design an efficient ideal interface for charge transfer/separation to reduce the consumption of photogenerated carriers is still the key to improve the photocatalytic performance of the heterojunction.

To achieve this goal, we designed an ultrathin Bi_2MoO_6 yolk@shell reactor loaded with MOF–derived ZnO clusters. The internal electric field generated by the loading of ZnO clusters controlled the accumulation and migration of electrons at the interface, enabling the reactor to promote photogenerated charge carrier separation through the transfer path of the S–scheme. Subsequently, PANI, a conducting polymer with widely delocalized π–conjugated electron system, was used to connect the reactor in tandem to establish a high–speed electron transport channel due to its high mobility of charge. Thus, the recombination of electron–holes was suppressed to the maximum extent, and the photogenerated carriers were accelerated migrate to the surface of the reactor to participate in the redox reaction. In addition, density functional theory (DFT) calculation was introduced to explore the charge transfer path and mechanism. Therefore, the performance of photocatalytic degradation of DC could be highly improved. It is reasonable to believe that such a yolk@shell reactor provides a new insight for improving the interfacial charge transfer of S–scheme heterojunction to enhance photocatalytic efficiency in the future.

2. Experimental section

All chemicals and reagents used in this study were commercially available and presented in Text S1. The detailed synthesis method of BiM/ZnC@PANI was shown in Text S2. Briefly, the hierarchical ultrathin Bi_2MoO_6 yolk@shell was prepared by typical solvothermal method. Then, nano ZIF–8 was loaded on ultrathin Bi_2MoO_6 nanosheets by chemical deposition, and transformed into ZnO clusters by subsequent heat treatment. Finally, PANI was uniformly wrapped on the BiM/ZnO–clusters yolk@shell reactor through simple immersion. The catalyst was prepared by chemical deposition of ZIF–8 at different time and different PANI dosage to optimize its performance. Catalyst characterization methods were described in Text S3. The catalytic mechanism of BiM/ZnC@PANI yolk@shell reactor for DC was systematically investigated. The experimental procedure and DFT calculation details were detailed in Text S4 and Text S5 in the Supporting Information.

3. Results and discussion

3.1. Synthesis and morphological characteristics of catalysts

The preparation strategy of the BiM/ZnC@PANI yolk@shell reactor was shown in Fig. 1a. Firstly, MOF–derived ZnO clusters (ZnO−Cs) were grown on ultrathin Bi_2MoO_6 nanosheets by wet chemistry and heat treatment. The growth mechanism of Bi_2MoO_6 yolk@shell was an Ostwald maturation process (Fig. S1a). It was well known that the euphotic structure was beneficial for decreasing density, and increasing light absorption and the number of active sites compared to solid counterparts [27]. This can also be proved by the difference in structure and performance of Bi_2MoO_6 with different solvothermal time in Fig. S1 and Text S6. The organic components in ZIF–8 gradually decompose to form ZnO with defects during the heat treatment stage. This process leads to the nucleation and crystallization of ZnO clusters uniformly distributed on the nanosheets to form heterojunctions. Finally, the reactor was coated with PANI by simple impregnation to construct the electron transfer channel. It can be observed in Fig. 1b that pure ZIF–8 was a rhomboid dodecahedron of about 50–70 nm. Bi_2MoO_6 was a yolk@shell with an average diameter of 1.65 μm and composed of self–assembled nanosheets (Fig. S1c inset). The morphology of Bi_2MoO_6 did not change after ZnO was loaded on the surface by calcination (Fig. 1c). Interestingly, the size of ZnO clusters could be easily adjusted by changing the deposition time of ZIF–8 (Fig. S2 and Text S7). However, the subsequent coating of PANI made the yolk@shell reactor wrapped with a thin polymer film, and the interface between the ultrathin nanosheets became slightly blurred (Fig. 1d), but too much PANI coating would cause adhesion between the reactors (Fig. S3). The transparent structure between yolk with shell could be clearly observed by TEM analysis of BiM/ZnC@PANI reactor (Fig. 1e). Fig. 1f shown that the ZnO clusters (about 2–5 nm, marked in red dashed lines) were highly dispersed on the ultrathin Bi_2MoO_6 nanosheets (inset). In the high–resolution TEM image of Fig. 1g, orthogonal lattice fringes of 0.274 and 0.270 nm could be observed, which were attributed to the orthogonal (200) and (060) planes of Bi_2MoO_6, respectively, indicating that the exposed (001) crystal plane [28]. Meanwhile, the lattice stripe of 0.247 nm in close contact with Bi_2MoO_6 could be attributed to ZnO (101). This result
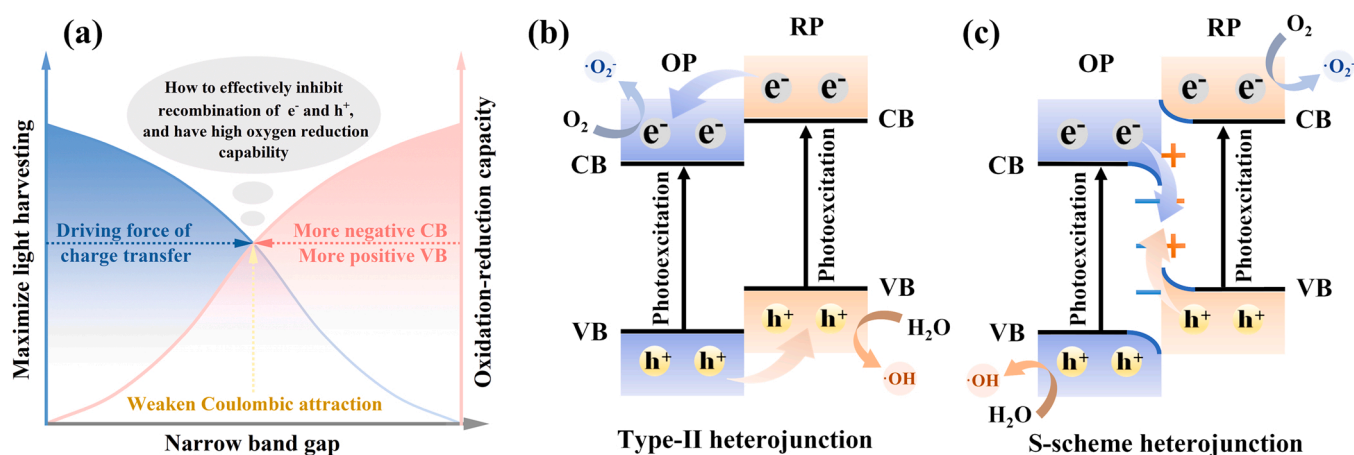
Scheme 1. Tradeoff between broad light absorption and redox capability (a); Schematic illustration of charge–carrier transfer pathways of conventional type–II (b) and S–scheme heterojunction (c).
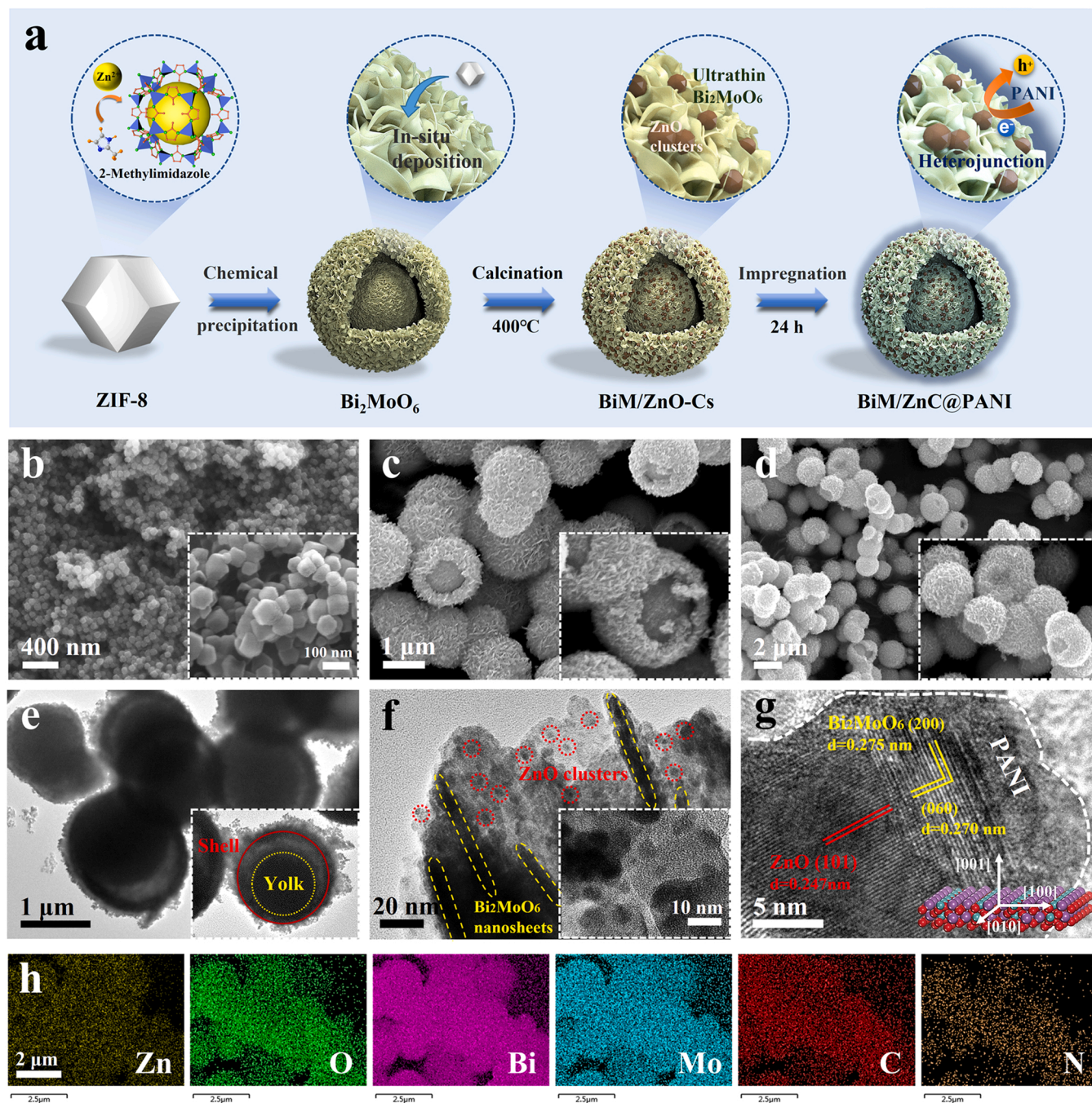
Fig. 1. Synthesis schematic illustration of BiM/ZnC@PANI yolk@shell reactor (a); SEM images of ZIF− 8 (b), BiM/ZnO−Cs (c) and BiM/ZnC@PANI (d); TEM and HR–TEM images of BiM/ZnC@PANI yolk@shell reactor (e–g), and element mapping (h) of BiM/ZnC@PANI (Zn, O, Bi, Mo, C and N).

confirmed that a large number of ZnO clusters were uniformly deposited on the (001) crystal plane of the ultrathin Bi_2MoO_6 nanosheet, and the obvious amorphous edges further indicated that PANI was deposited on the yolk@shell reactor. The element mapping shown that Bi, Mo, Zn, O, C and N elements were uniformly distributed (Fig. 1h). The average nanosheet thickness of BiM/ZnC@PANI with 001 crystal plane was determined by AFM to be 3.5 nm, which was in good agreement with the TEM results (Fig. S4). It is worth mentioning that the carriers in the ultrathin structure migrated to the surface faster than those in the bulk structure because their migration distance was the atomic thickness [29]. To sum up, the ultrathin Bi_2MoO_6 was uniformly loaded with MOF–derived ZnO clusters coated with PANI on the exposed 001 crystal plane, which means that the yolk@shell reactor was successfully

synthesized.

3.2. Analysis of phase, optical properties and catalytic performance

The crystal structure of the catalyst was investigated by XRD (Fig. 2a). The diffraction peak of the prepared ultrathin Bi_2MoO_6 can be well correlated with the standard pattern (JCPDS No. 72–1524), indicating that it has a high crystallinity. BiM/ZnO–Cs can also see the diffraction peaks of ZnO (JCPDS No. 89–0510) at 31.9° and 36.4°, which correspond to the (100) and (101) planes of ZnO, respectively. Among them, the relatively weak diffraction peak of ZnO was due to the low content and the small ZnO clusters, so the effective crystal structure cannot be detected [30]. In addition, the diffraction peak intensity of
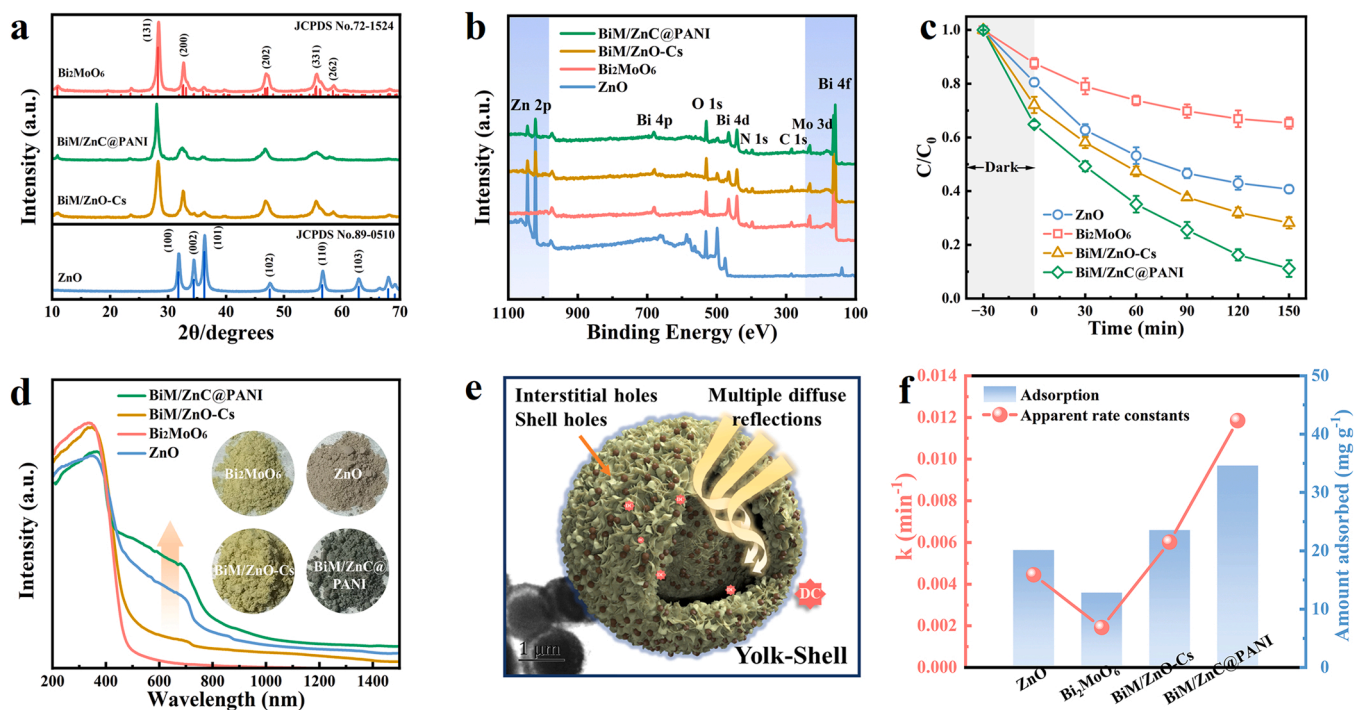
Fig. 2. XRD patterns (a), full XPS spectrum (b) and photocatalytic degradation curve (c) of catalysts; Reaction Conditions: [DC] = 10 mg L^{-1}, [volume] = 50 mL, [catalyst] = 5 mg. UV–vis diffuse reflectance spectra (d), the **inset** is the photos of the catalysts; Schematic diagram of light diffuse reflection in yolk@shell reactor (e); Maximum adsorption capacity and degradation reaction rate constants k of catalysts (f).

ZnO gradually became stronger with the increased of ZIF–8 deposition time, indicating the increased of the loading (Fig. S5a). However, the XRD pattern of BiM/ZnC@PANI did not change significantly, and the intensity was slightly reduced after the subsequent coating of PANI, indicating that the PANI had no obvious effect on the lattice structure and uniformity of BiM/ZnO–Cs (Fig. S5b) [31]. The surface chemical state of the catalysts was studied by X–ray photoelectron spectroscopy (XPS). Bi, Mo and Zn elements can be observed simultaneously in the full XPS spectrum of BiM/ZnO–Cs. While the presence of PANI can be easily confirmed by the increased atomic concentrations of C and N in BiM/ZnC@PANI (Fig. 2b and Table S1). Meanwhile, the N$_2$ adsorption−desorption isotherms and detailed parameters of the catalyst were shown in Fig. S6 and Table S2. It can be observed that a typical type IV isotherms, indicating a homogeneous mesoporous structure. The range of 1.5–3.0 nm and 10–100 nm can be attributed to shell pore channels and gap pores, respectively [32]. The variation of surface area and pore size also proved the loading of ZnO clusters and the coating of PANI.

The photocatalytic ability of the catalysts was investigated by degradation DC in visible light. Fig. 2c shown that ZnO transformed by ZIF–8 had better performance than Bi$_2$MoO$_6$. After a small amount of ZnO cluster loading on the ultrathin Bi$_2$MoO$_6$, it had better performance, and the degradation capacity was further improved by subsequent PANI coating. However, excessive amounts of ZnO and PANI will lead to a decrease in the photodegradation rate of DC, which may be due to blocking the active site of the reactor and hindering the charge transfer to the surface (Fig. S7). The visible light absorption ability of catalysts may lead to the difference of photocatalytic performance. Therefore, the optical properties of the catalysts were determined by UV–vis diffuse reflectance spectra (Fig. 2d). Individual Bi$_2$MoO$_6$ exhibited an obvious absorption edge from 500 nm to 800 nm, showing the great visible light response performance of the ultrathin Bi$_2$MoO$_6$ yolk@shell (Fig. 2e). The visible light absorption intensity of BiM/ZnO–Cs heterojunctions was significantly enhanced, and the heterojunction darkened with PANI coating (inset of Fig. 2d). PANI can be used as a good visible photosensitizer and charge separation center and hole transport layer for BiM/

ZnO–Cs, which enhanced the photocatalytic performance of the yolk@shell reactor [33,34]. The band gap of Bi$_2$MoO$_6$ yolk@shell was about 2.83 eV, while ZnO produced by calcination of ZIF–8 had a narrower band gap (~ 2.53 eV) than conventional ZnO (~ 3.2) (Fig. S8). This may be due to the insufficient calcination of organic matter in ZIF–8 leading to the formation of oxygen vacancies [35]. The band structures of Bi$_2$MoO$_6$, pure ZnO and ZnO with oxygen vacancies were studied by DFT in order to understand the change of band gap position (Fig. S9 and Text S8). The appearance of oxygen vacancies can not only increase the band density, but also create more vacancies extending to regions slightly above the Fermi level. Meanwhile, ZnO was endowed with an intermediate gap state, which lead to an additional extension of the valence band. And electron was more easily excited by light to jump into higher energy regions and induced more extensive light absorption [36]. The electron paramagnetic resonance (EPR) also demonstrated the existence of defects in the prepared catalysts (Fig. S10). Therefore, the loading MOF–derived ZnO clusters and coating photosensitizer PANI led to a narrower band gap and wider visible light response capability of the Bi$_2$MoO$_6$ yolk@shell reactor.

In addition to optical characteristics, reactor also had great adsorption capacity in the dark reaction process (Fig. S11 and Text S9). The adsorption of DC reached equilibrium within 30 min, which meant that the adsorption did not interfere with the subsequent analysis of photocatalytic results, and the maximum adsorption capacity (q_{max}) reached 47.4 mg g^{-1} (Tables S3 and S4). Due to its great adsorption capacity, low concentration of DC can be removed by adsorption more than 80%, and even higher concentration can be degraded by more than 55% with less catalyst. (Fig. S12). The adsorption can be attributed to the ionic form of DC and the large number of hydroxyl groups (pK$_a$=3.0, 8.0, and 9.2), which facilitates BiM/ZnC@PANI attraction through the layered porous structure and electrostatic attraction (Fig. S13). Therefore, BiM/ZnC@PANI had great dark adsorption performance and degradation rate k, as well as good DC mineralization ability, and the total organic carbon (TOC) removal rate was 57% within 150 min (Fig. 2f and S14).

3.3. Study on charge transfer characteristics

Electron transfer was one of the prerequisites for the charge carrier to reach the catalyst surface and generate reactive oxygen species (ROS) with high oxidation capacity. Therefore, the differential charge distribution at the interface was simulated by density functional theory (DFT) to explore the difference in electronic structure between ultrathin Bi_2MoO_6 with ZnO cluster and PANI. Bi_2MoO_6 with (001) exposed crystal was selected as the model due to HRTEM indication (Fig. S15). As shown in Fig. 3a, the loading of ZnO clusters on the (001) crystal of Bi_2MoO_6 had a strong interaction at the interface leading to the aggregation of more electrons (yellow and blue represent charge depletion and accumulation). The increased charge density around the ZnO cluster shifted and accumulated at the interface, leading to the generation of an internal electric field (IEF) to accelerate the separation of charge carriers [37,38]. However, the subsequent coating of PANI provided a high–speed channel for efficient electron transport. In this way, electrons were preferentially transferred to PANI with high conductivity to effectively improve the surface–interface migration and catalytic activity of photogenerated charge carriers [31]. The total density of states (DOS) calculated in Fig. 3b shown that new DOS appear in BiM/ZnC@PANI bandgap, and the introduction of Zn and C atoms in ZnO clusters and

PANI significantly increases the valence band maximum. Thus, more electrons in BiM/ZnC@PANI can be photoexcited to the conduction band in visible light, and photocatalytic activity can also be improved due to easier electron transitions [39]. Meanwhile, the high–resolution XPS spectra of Bi 4 f and Mo 3d shown changes in binding energy, which can be attributed to the interaction (strong electronic interaction and chemical bonding) between Bi_2MoO_6, ZnO clusters and PANI (Fig. 3c and d). Therefore, a shift of the Bi 4 f and Mo 3d peaks toward lower wave–numbers can be observed after loading ZnO clusters, indicating that the increase in electron density between Bi_2MoO_6 and ZnO clusters led to the generation of the IEF. Then there were some positive shift after the heterojunction coating the highly conductive PANI. This implied a transfer of electrons from Bi_2MoO_6 and ZnO clusters to PANI, indicating the formation of an intimate interface with strong interactions. Therefore, PANI was essential for promoting the migration and separation of charge carriers and photocatalytic activity, which was consistent with the results of DFT simulations. Zn 2p shown a spin–orbit split of 23.1 eV, confirming that Zn^{2+} in reactor (Fig. S16a). The changes of O 1 s high–resolution XPS spectra were similar to those of Bi 4 f and Mo 3d (Fig. S16b), and the existence of oxygen defects in the material can be observed, which was also consistent with the results of EPR (Fig. S9). The C1s spectra were shown in Fig. S16c, the binding energies of 288.9,
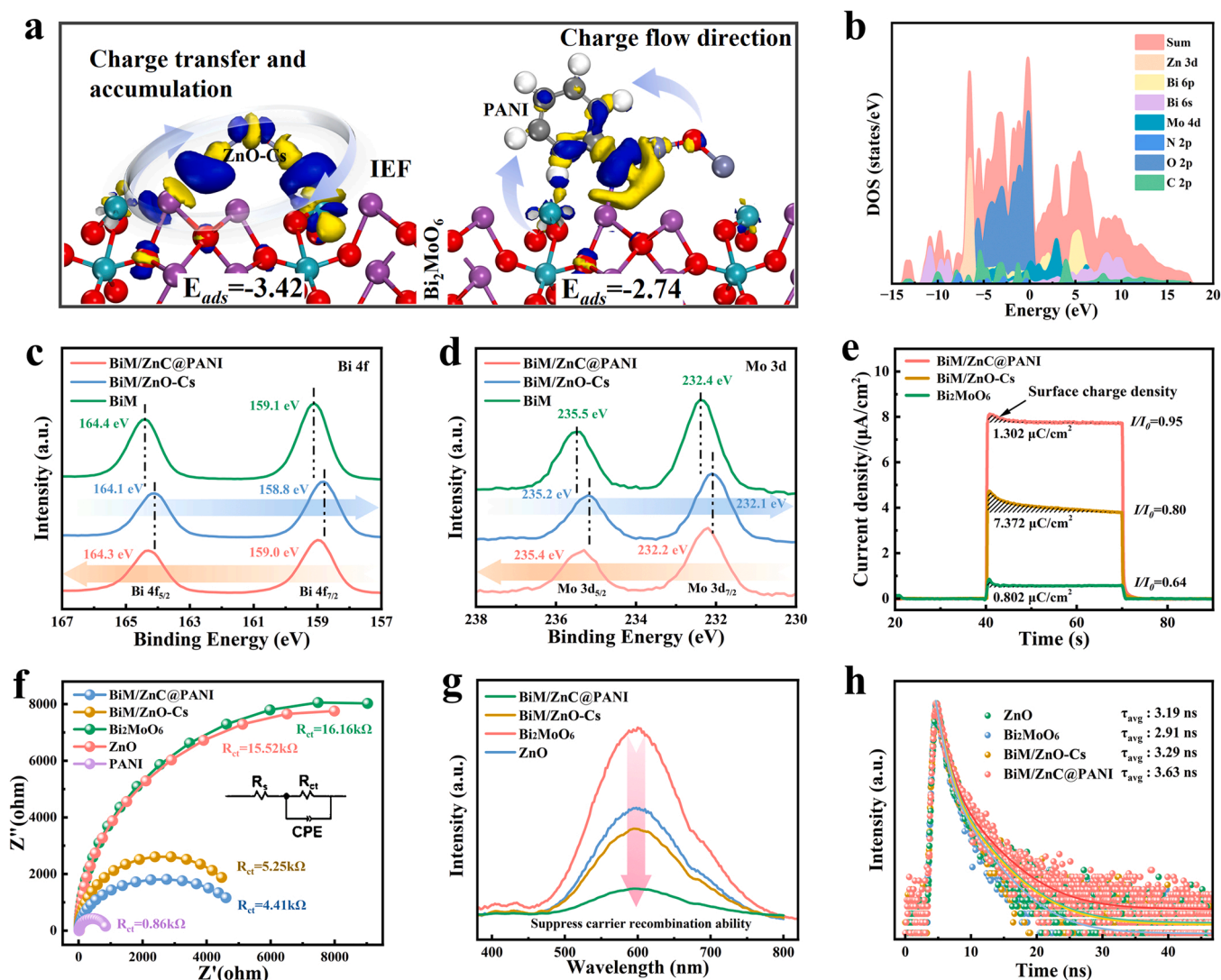
Fig. 3. The charge density difference of interface. Blue and yellow indicate charge accumulation and depletion, respectively (a); PDOS of the optimized configurations of BiM/ZnC@PANI (b); XPS spectra and fitting curves of Bi 4 f (c) and Mo 3d (d); The surface charge density (e), EIS Nyquist plots (f), PL characterizations (g) and TRPL (h) spectroscopy of catalysts.

285.5 and 284.6 eV correspond to the carbon residue converted from ZIF–8 to ZnO and C–N and C–C of PANI, respectively.

In addition, the IEF of Bi_2MoO_6, BiM/ZnO–Cs and BiM/ZnC@PANI as the driving force for charge transfer at the interface were measured by a model developed by Kanata et al. (Fig. S17 and Text S10) [40–43]. As shown in Fig. 3e, the surface charge density of the catalyst was measured by subtracting the steady–state integral of the transient photocurrent density measured over time [44]. The surface charge density of BiM/ZnO–Cs heterojunction was significantly higher than that of Bi_2MoO_6. Meanwhile, the IEF of BiM/ZnO–Cs and BiM/ZnC@PANI were 12.4 and 3.9 times higher than that of Bi_2MoO_6, respectively, which can significantly accelerate the interfacial charge separation (Fig. S17). However, it was worth noting that the surface charge density of BiM/ZnC@PANI was reduced, i/i_0 approaching to 1, indicating that no charge accumulation at the electrode, and the recombination of charge carriers was significantly reduced [45]. In addition, the electrochemical impedance spectroscopy (EIS) of PANI showed the lowest interfacial charge resistance (R_{ct}~0.86 kΩ) of all electrodes (Fig. 3f), indicating that electrons can be easily transferred out through PANI [46]. At the same time, BiM/ZnC@PANI shown a smaller arc radius from the Nyquist curve fitted by the equivalent circuit, which implied faster electron separation and lower transmission resistance. Thanks to this, BiM/ZnC@PANI had the strongest photocurrent signal (Fig. S18). These results quantitatively demonstrated that IEF generated by ZnO clusters and the high conductivity of PANI had significant effect on the dynamics of carrier separation/transfer, providing a strong driving force for photogenic charge carrier, and it coincided with the previous DFT results. This result was further confirmed by PL spectroscopy, which showed that BiM/ZnC@PANI inhibited carrier recombination more significantly than other catalysts (Fig. 3g). Meanwhile, nanosecond time–resolved fluorescence attenuation experiments revealed the recombination time of photogenerated electron–hole pairs. Fig. 3h clearly showed the accelerated photoluminescence decay of the catalysts, and the calculated average radiation lifetimes of ZnO, Bi_2MoO_6, BiM/ZnO–Cs and BiM/ZnC@PANI were 3.19, 2.91, 3.29 and 3.63 ns, respectively (Table S5). The extended lifetime was attributed to the loading of ZnO clusters and the coating of PANI, which greatly enhanced the charge transfer and exciton dissociation leading to slower decay rate and longer lifetime.

3.4. Exploration of carrier transfer direction and photocatalysis mechanism

The path and direction of carrier transport during photoexcitation were further explored. VB–XPS was used to directly determine the VB position of the semiconductor (Fig. S19). The CB positions of Bi_2MoO_6 and ZnO were about –1.08 and 0.24 combined with the previously obtained band gap values. The slope of the Mott–Schottky curve shown that Bi_2MoO_6 and ZnO were N–type semiconductors, while PANI was P–type semiconductors (Fig. S20). As shown in Fig. 4a, the work function calculated by DFT shown that Bi_2MoO_6 (4.61 eV) was significantly higher than ZnO (6.72 eV), and the Fermi energy level difference between them determined that IEF must occur at the contact interface [47]. According to the above results, the schematic diagram of the semiconductor band structure was shown in Fig. 4b. The VB of Bi_2MoO_6 and CB of ZnO were 1.75 and 0.24 eV, which were not sufficient for the activation of •OH (H_2O/•OH 2.27 eV vs NHE) and $•O_2^-$ (O_2/$•O_2^-$ –0.28 eV vs NHE) [33]. The EPR spectra of DMPO– of Bi_2MoO_6 and ZnO also supported this result (Fig. 4c and d). However, the BiM/ZnO–Cs heterojunction can simultaneously produce •OH, $•O_2^-$ and $^1O_2$, which was different from the transfer path of type–II heterojunction. Therefore, S–scheme heterojunction can vividly describe the charge carrier transfer route by analyzing the above results [48,49]. Specifically, as shown in Fig. 4b, when Bi_2MoO_6 was in contact with ZnO, e^- would be transferred to the ZnO cluster interface due to the higher Fermi energy level of Bi_2MoO_6. As a result, the side of Bi_2MoO_6 was positively charged due to the depletion of e^-, while the side of ZnO was negatively charged due to the accumulation of e^-, resulting in an IEF at the interface. At the same time, the energy bands at the interface of Bi_2MoO_6 and ZnO cluster were bent up and down respectively to align the Fermi levels to the same level. Under the photoexcitation, the photogenerated e^- were driven by the IEF from CB of ZnO to VB of Bi_2MoO_6. In addition, the Coulomb attraction between the e^- in ZnO and the h^+ in Bi_2MoO_6 and the curved energy band were also conducive to this charge transfer [19]. ZnO
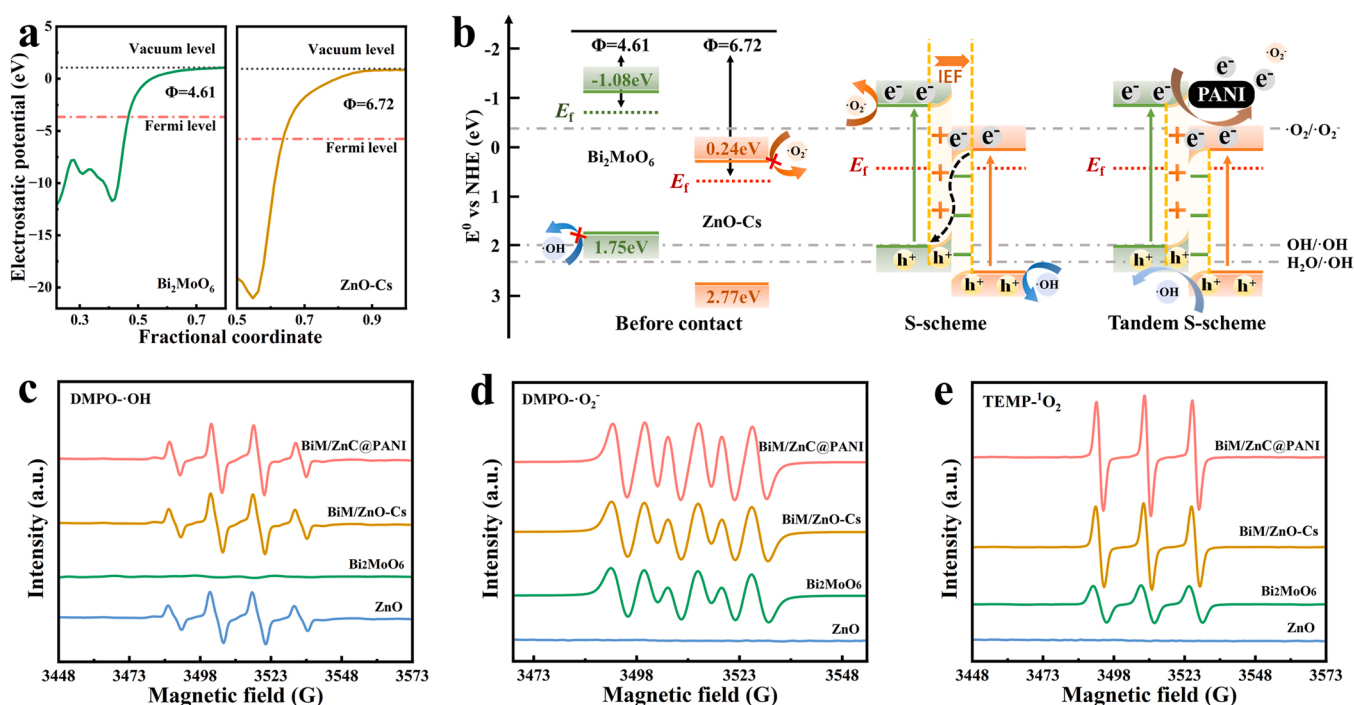

Fig. 4. Electrostatic potentials of Bi_2MoO_6 and ZnO (a); S–scheme transfer mechanism with PANI high speed charge transfer channel (b); EPR signals for DMPO–•OH (c), DMPO–$•O_2^-$ (d) and TMPO–$^1O_2$ (e);.

clusters can be used as electronic transfer stations to achieve more efficient charge migration and accumulation. It was convincing that the introduction and coordination of PANI between heterojunction will establish channels for efficient interlayer charge carrier transport. The highly conductive PANI distributed on the BiM/ZnO−Cs can make it easier for e^- migrating to the surface to participate in the catalytic reaction, so as to inhibit the consumption of e^- return and h^+ recombination, enabling tandem between Bi_2MoO_6 and ZnO clusters [50]. Finally, this tandem S–scheme system together achieved carrier transfer and gave BiM/ZnC@PANI extremely high redox capacity. Therefore, BiM/ZnC@PANI had a stronger ability to generate $\bullet OH$, $\bullet O_2^-$ and $^1O_2$, consistent with enhanced interfacial charge transfer (Fig. 4c–e).

Therefore, a small amount of BiM/ZnC@PANI (0.1 mg L^{-1}) was required and can degrade more than 90% of DC within 150 min, with a maximum rate constant of 0.012 min^{-1} (Fig. 5a). Meanwhile, it had good adsorption and degradation effect on other typical broad–spectrum antibiotics, such as tetracycline (TC), oxytetracycline (OTC), chlortetracycline (CTC), levofloxacin (LVF) (Fig. 5b). Compared with other tetracycline degradation catalysts, BiM/ZnC@PANI had better performance under the condition of small dosage (Table S6). However, the removal ability of sulfamethoxazole (SMX) was poor, which may be due to the stubbornness of SMX [51], the small amount of catalyst added and the short degradation time. The pH of the solution had a certain effect on the degradation of DC (Fig. 5c and S21), which may be due to the surface charge difference between reactor and DC (pK_a = 3.0, 8.0 and 9.2) [52].

The degradation of DC by BiM/ZnC@PANI was less affected by coexisting ions (Fig. S22 and Text S11). The photocatalytic reusability and repeatability of the BiM/ZnC@PANI yolk@shell reactor were verified by repeated experiments (Fig. 5d). The characteristics of XRD, SEM and XPS remained basically unchanged after the cycle (Fig. S23). At the same time, the concentrations of Zn^{2+}, Bi^{3+} and Mo^{6+} ions in the circulating solution were low by inductively coupled plasma mass spectrometry (ICP–MS) (Table S7), which demonstrated that the BiM/ZnC@PANI yolk@shell reactor had good chemical stability. ROS capture experiments were further conducted to clarify the role of ROS in photocatalytic degradation of DC (Fig. 5e). The results showed that $\bullet O_2^-$ was the main active species, and $^1O_2$ and h^+ also played an auxiliary role, while $\bullet OH$ only contributed a little to the degradation of DC. Meanwhile, the analysis of chronopotentiometry and chronoamperometry in Fig. 5f shown that the potential and photocurrent increase sharply after illumination and then tend to be stable. It indicated the exchange of e^- at the BiM/ZnC@PANI interface and induced a high redox potential. However, the e^- in the system were extracted and consumed with the addition of DC solution, which made the intensity of the e^- signal instantly decrease, because the e^- participated in the generation of ROS [53].

3.5. Excellent degradation pathway of yolk@shell reactor

The possible pathway and mechanism of photocatalytic degradation DC were deduced by ROS capture experiment, HPLC–MS and DFT calculation (Fig. 6 and S24). The Fukui indices of electrophilic (f^-), radical (f^0) and nucleophilic (f^+) can theoretically revealed the reactive sites of DC molecules (Fig. 6a). In general, h^+ and $^1O_2$ shown high selectivity for electron–rich regions, and thus were easy to attack with high f^- sites. f^0 can reflect the regional selectivity of radical species ($\bullet O_2^-$ and $\bullet OH$) [54]. The highest occupied molecular orbital (HOMO) of DC indicated that the e^- binding was looser in the methyl region near N_{25}, which made it easy to lose e^- (Fig. 6b). The lowest unoccupied molecular orbital (LUMO) had a strong affinity for e^- in the hydroxyl functional group region, and had the property of e^- acceptor. The possible degradation pathway of DC was shown in Fig. 6c. First, N_{25} (f^- = 0.235), C_{31} (f^- = 0.054) and C_{32} (f^- = 0.051) in DC had high f^-, so they were theoretically vulnerable to h^+ and $^1O_2$ to demethylate, producing intermediates D1 and D2, which were further hydroxylated to produce D3 [55]. O_{20} and C_7 had high f^0 and f^+ as well as electrophilic hydroxyl regions, so they were vulnerable to attack by $\bullet O_2^-$ and $\bullet OH$ to form D4
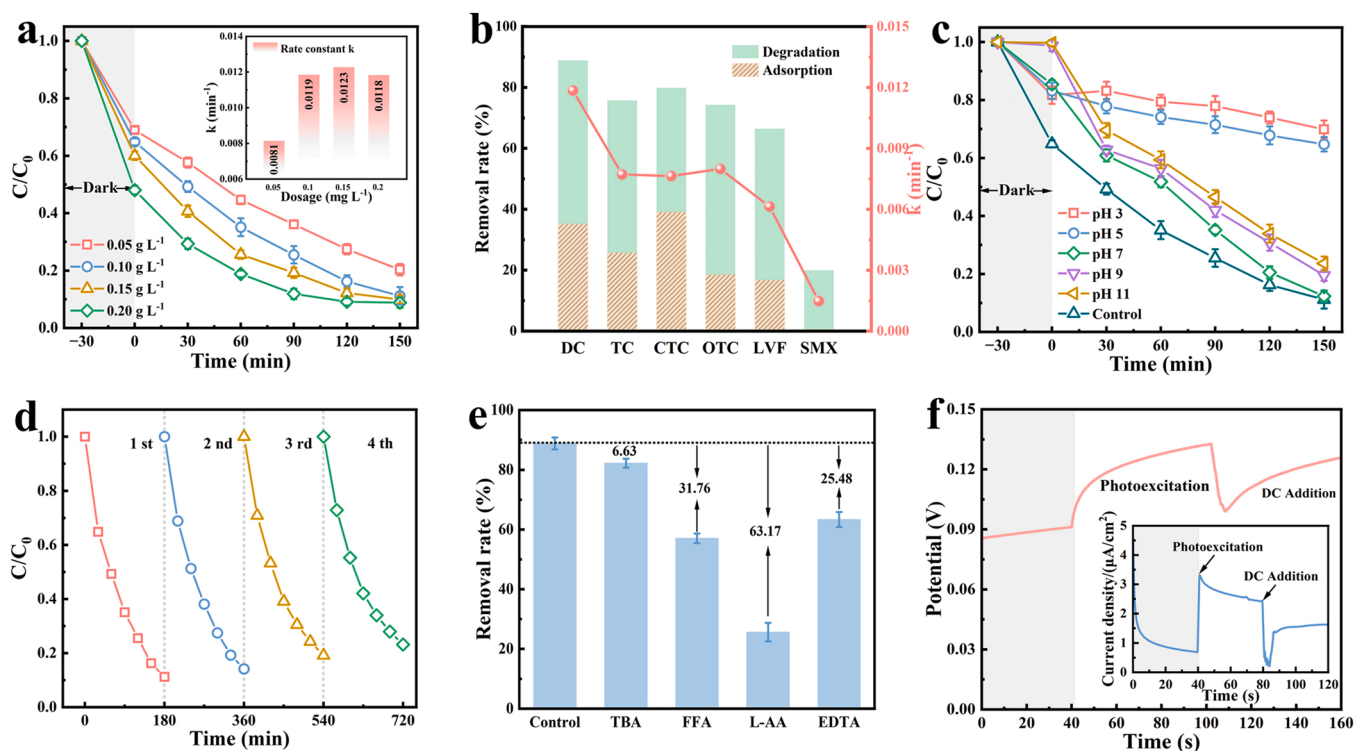
Fig. 5. Catalytic degradation curve and the reaction rate constants k **(inset)** of dosage (a); Adsorption and degradation of typical antibiotics (b); The different pH (c) and recycle of degradation DC (d) by BiM/ZnC@PANI yolk@shell reactor; The degradation of DC containing different quenchers (e). Reaction Conditions: [antibiotic] = 10 mg L^{-1}, [volume] = 50 mL, [catalyst] = 5 mg. Chronopotentiometry and chronoamperometry **(inset)** curve of the BiM/ZnC@PANI electrode with photoexcitation and adding DC (f).

a — Calculated Fukui index of DC

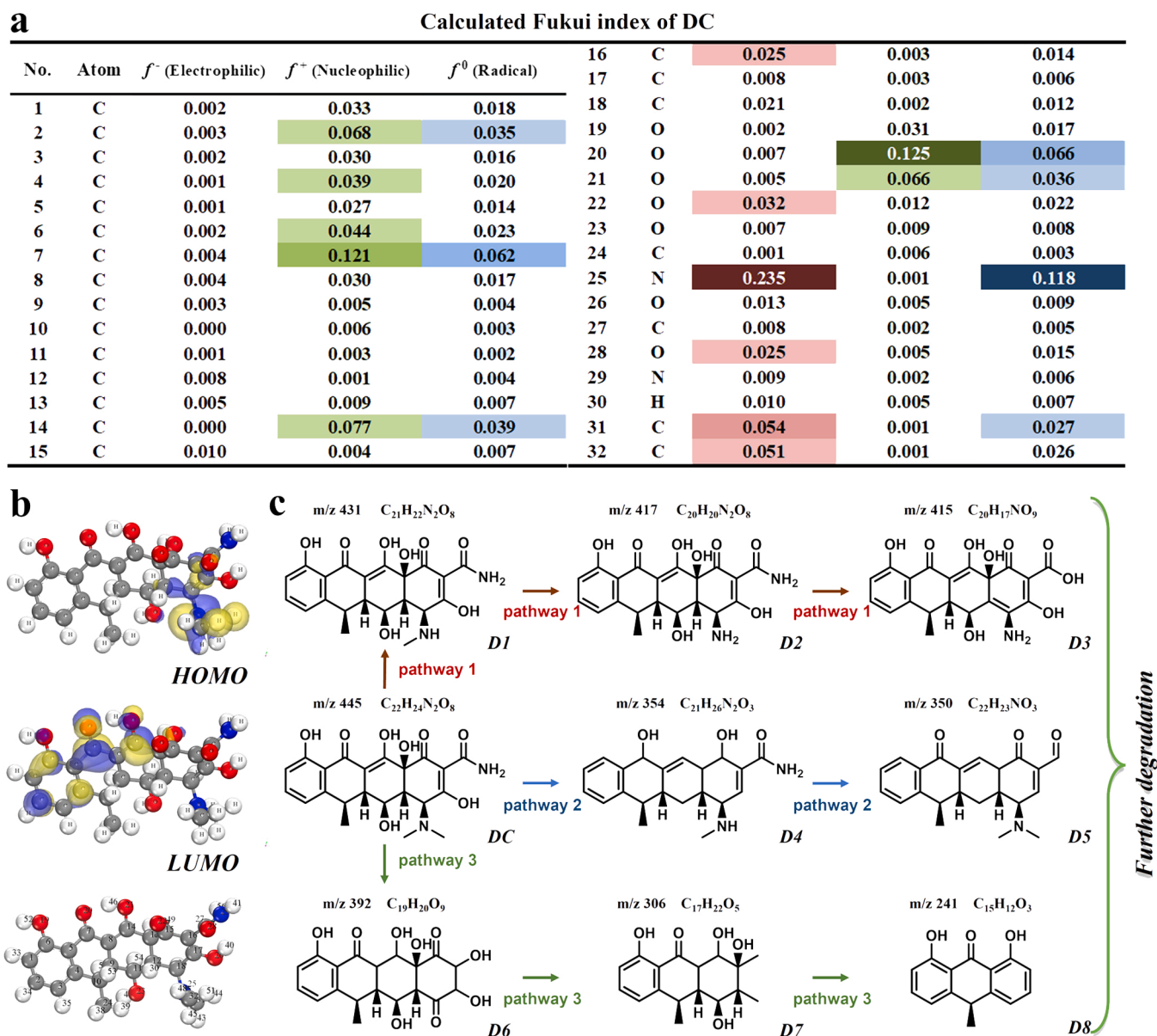| No.	Atom	f^- (Electrophilic)	f^+ (Nucleophilic)	f^0 (Radical)
1	C	0.002	0.033	0.018
2	C	0.003	0.068	0.035
3	C	0.002	0.030	0.016
4	C	0.001	0.039	0.020
5	C	0.001	0.027	0.014
6	C	0.002	0.044	0.023
7	C	0.004	0.121	0.062
8	C	0.004	0.030	0.017
9	C	0.003	0.005	0.004
10	C	0.000	0.006	0.003
11	C	0.001	0.003	0.002
12	C	0.008	0.001	0.004
13	C	0.005	0.009	0.007
14	C	0.000	0.077	0.039
15	C	0.010	0.004	0.007
16	C	0.025	0.003	0.014
17	C	0.008	0.003	0.006
18	C	0.021	0.002	0.012
19	O	0.002	0.031	0.017
20	O	0.007	0.125	0.066
21	O	0.005	0.066	0.036
22	O	0.032	0.012	0.022
23	O	0.007	0.009	0.008
24	C	0.001	0.006	0.003
25	N	0.235	0.001	0.118
26	O	0.013	0.005	0.009
27	C	0.008	0.002	0.005
28	O	0.025	0.005	0.015
29	N	0.009	0.002	0.006
30	H	0.010	0.005	0.007
31	C	0.054	0.001	0.027
32	C	0.051	0.001	0.026

Fig. 6. Calculated Fukui index (a), HOMO and LUMO of DC (b) and possible transformation pathways of DC by BiM/ZnC@PANI yolk@shell reactor (c).

and D5 through functional group cleavage [56]. In the process of reaction, DC can also be formed into D6, D7 and D8 by gradual ring opening and bond breaking and dihydroxylation [57]. These complex structures were further oxidized to produce simpler organic compounds, and eventually the intermediates were broken down into H_2O and CO_2. Therefore, based on oxidation product identification, Fukui index and HOMO and LUMO analysis, three possible reaction pathways of DC in BiM/ZnC@PANI yolk@shell reactor, such as demethylation, functional group cleavage and hydroxylation reactions, had been identified. The developmental toxicity of DC and corresponding intermediates was evaluated using the Toxicity Estimation Software (T.E.S.T.). DC had a developmental toxicity index of 0.87, which was classified as a developmental poison and can caused interference in larval development. However, the developmental toxicity values of most degradation products decreased in the process of DC photocatalytic degradation (Fig. S25). The results shown that the photocatalytic process of BiM/ZnC@PANI yolk@shell reactor can not only effectively degrade DC, but also reduce its ecotoxicity.

4. Conclusions

In conclusion, we constructed a yolk@shell reactor with MOF derived ZnO clusters coated with PANI on the 001 crystal of ultrathin Bi_2MoO_6. The path and mechanism of carrier transfer were further investigated through the analysis of optical response, differential charge and multiple characterization. ZnO clusters can be used as intermediate stations for electron transfer, enabling the accumulation and migration of photogenerated carriers at the interface. The highly conductive polymer PANI was connected in tandem with heterojunctions to establish high–speed electron transfer channels and promoted directional electron transport. Charge carrier recombination (e^- and h^+) was restricted due to the superior S–scheme migration path and high–speed carrier transport channels. And the charge transfer from the body to the surface can be promoted, and ROS ($\bullet OH$, $\bullet O_2^-$ and $^1O_2$) with high oxidation capacity can be generated to participate in the surface redox reaction. In addition, the degradation pathway of DC was calculated and analyzed by HPLC−MS combined with DFT theory. This study will provide a new insight into the design and construction of a yolk@shell reactor to improve interfacial charge transfer and enhance

photocatalytic efficiency of S–scheme heterojunction.

CRediT authorship contribution statement

Aiwen Wang: Conceptualization, Methodology, Software, Data curation, Writing – original draft, Visualization, Investigation, Software, Validation, Writing – review & editing. **Wei Wang:** Formal analysis, Funding acquisition. **Jiaxin Ni:** Formal analysis Visualization. **Dongqing Liu:** Visualization. **Dongmei Liu:** Project administration, Conceptualization, Formal analysis, Funding acquisition, Writing – review & editing, Supervision. **Jun Ma:** Formal analysis, Investigation. **Xuebin Jia:** Project administration, Supervision.

Declaration of Competing Interest

The authors declare that they have no known competing financial interests or personal relationships that could have appeared to influence the work reported in this paper.

Data Availability

Data will be made available on request.

Acknowledgements

Appendix A. Supporting information

Supplementary data associated with this article can be found in the online version at doi:10.1016/j.apcatb.2023.122492.

References

[1] Y. Shi, Z. Yang, L. Shi, H. Li, X. Liu, X. Zhang, J. Cheng, C. Liang, S. Cao, F. Guo, X. Liu, Z. Ai, L. Zhang, Surface boronizing can weaken the excitonic effects of BiOBr nanosheets for efficient O_2 activation and selective NO oxidation under visible light irradiation, Environ. Sci. Technol. 56 (2022) 14478–14486.

[2] X. Xu, N. Yang, P. Wang, S. Wang, Y. Xiang, X. Zhang, X. Ding, H. Chen, Highly intensified molecular oxygen activation on Bi@Bi_2MoO_6 via a metallic Bi-coordinated facet-dependent effect, ACS Appl. Mater. Interfaces 12 (2020) 1867–1876.

[3] Z. Yin, M. Tordjman, Y. Lee, A. Vardi, R. Kalish, J.A. del Alamo, Enhanced transport in transistor by tuning transition-metal oxide electronic states interfaced with diamond, Science Advances, 4 eaau0480.

[4] X. Feng, W. Zhang, H. Deng, Z. Ni, F. Dong, Y. Zhang, Efficient visible light photocatalytic NOx removal with cationic Ag clusters-grafted $(BiO)_2CO_3$ hierarchical superstructures, J. Hazard. Mater. 322 (2017) 223–232.

[5] J. Low, J. Yu, M. Jaroniec, S. Wageh, A.A. Al-Ghamdi, Heterojunction photocatalysts, Adv. Mater. 29 (2017) 1601694.

[6] R.A. Marcus, Electron transfer reactions in chemistry: theory and experiment (nobel lecture), Angew. Chem. Int. Ed. Engl. 32 (1993) 1111–1121.

[7] J. Zhang, C. Shao, X. Li, J. Xin, R. Tao, Y. Liu, Assembling n-Bi_2MoO_6 nanosheets on electrospun p-$CuAl_2O_4$ hollow nanofibers: enhanced photocatalytic activity based on highly efficient charge separation and transfer, ACS Sustain. Chem. Eng. 6 (2018) 10714–10723.

[8] S. Wang, X. Ding, X. Zhang, H. Pang, X. Hai, G. Zhan, W. Zhou, H. Song, L. Zhang, H. Chen, J. Ye, In situ carbon homogeneous doping on ultrathin bismuth molybdate: a dual-purpose strategy for efficient molecular oxygen activation, Adv. Funct. Mater. 27 (2017) 1703923.

[9] Y. Zheng, T. Zhou, X. Zhao, W.K. Pang, H. Gao, S. Li, Z. Zhou, H. Liu, Z. Guo, Atomic interface engineering and electric-field effect in ultrathin Bi_2MoO_6 nanosheets for superior lithium ion storage, Adv. Mater. 29 (2017) 1700396.

[10] B. Zhang, J. Li, Y. Gao, R. Chong, Z. Wang, L. Guo, X. Zhang, C. Li, To boost photocatalytic activity in selective oxidation of alcohols on ultrathin Bi_2MoO_6 nanoplates with Pt nanoparticles as cocatalyst, J. Catal. 345 (2017) 96–103.

[11] Z. Xing, W. Kong, T. Wu, H. Xie, T. Wang, Y. Luo, X. Shi, A.M. Asiri, Y. Zhang, X. Sun, Hollow Bi_2MoO_6 sphere effectively catalyzes the ambient electroreduction of N_2 to NH_3, ACS Sustain. Chem. Eng. 7 (2019) 12692–12696.

[12] R. Kashfi-Sadabad, S. Yazdani, A. Alemi, T.D. Huan, R. Ramprasad, M.T. Pettes, Block copolymer-assisted solvothermal synthesis of hollow Bi_2MoO_6 spheres substituted with samarium, Langmuir 32 (2016) 10967–10976.

[13] X. Xu, X. Ding, X. Yang, P. Wang, S. Li, Z. Lu, H. Chen, Oxygen vacancy boosted photocatalytic decomposition of ciprofloxacin over Bi_2MoO_6: Oxygen vacancy engineering, biotoxicity evaluation and mechanism study, J. Hazard. Mater. 364 (2019) 691–699.

[14] Y. Chen, W. Yang, S. Gao, C. Sun, Q. Li, Synthesis of $Bi2MoO6$ nanosheets with rich oxygen vacancies by postsynthesis etching treatment for enhanced photocatalytic performance, ACS Appl. Nano Mater. 1 (2018) 3565–3578.

[15] X. Wu, J.N. Hart, X. Wen, L. Wang, Y. Du, S.X. Dou, Y.H. Ng, R. Amal, J. Scott, Improving the photo-oxidative performance of Bi_2MoO_6 by harnessing the synergy between spatial charge separation and rational Co-catalyst deposition, ACS Appl. Mater. Interfaces 10 (2018) 9342–9352.

[16] E. Vesali-Kermani, A. Habibi-Yangjeh, H. Diarmand-Khalilabad, S. Ghosh, Nitrogen photofixation ability of g-C_3N_4 nanosheets/Bi_2MoO_6 heterojunction photocatalyst under visible-light illumination, J. Colloid Interface Sci. 563 (2020) 81–91.

[17] C. Wang, M. Cai, Y. Liu, F. Yang, H. Zhang, J. Liu, S. Li, Facile construction of novel organic–inorganic tetra (4-carboxyphenyl) porphyrin/Bi_2MoO_6 heterojunction for tetracycline degradation: Performance, degradation pathways, intermediate toxicity analysis and mechanism insight, J. Colloid Interface Sci. 605 (2022) 727–740.

[18] Q. Xu, L. Zhang, J. Yu, S. Wageh, A.A. Al-Ghamdi, M. Jaroniec, Direct Z-scheme photocatalysts: principles, synthesis, and applications, Mater. Today 21 (2018) 1042–1063.

[19] L. Zhang, J. Zhang, H. Yu, J. Yu, Emerging S-scheme photocatalyst, Adv. Mater. 34 (2022) 2107668.

[20] Q. Xu, L. Zhang, B. Cheng, J. Fan, J. Yu, S-scheme heterojunction photocatalyst, Chem 6 (2020) 1543–1559.

[21] Q. Li, W. Zhao, Z. Zhai, K. Ren, T. Wang, H. Guan, H. Shi, 2D/2D Bi_2MoO_6/g-C_3N_4 S-scheme heterojunction photocatalyst with enhanced visible-light activity by Au loading, J. Mater. Sci. Technol. 56 (2020) 216–226.

[22] P. Xia, S. Cao, B. Zhu, M. Liu, M. Shi, J. Yu, Y. Zhang, Designing a 0D/2D S-scheme heterojunction over polymeric carbon nitride for visible-light photocatalytic inactivation of bacteria, Angew. Chem. Int. Ed. 59 (2020) 5218–5225.

[23] C. Cheng, B. He, J. Fan, B. Cheng, S. Cao, J. Yu, An inorganic/organic S-scheme heterojunction H_2-production photocatalyst and its charge transfer mechanism, Adv. Mater. 33 (2021) 2100317.

[24] X. Li, B. Kang, F. Dong, Z. Zhang, X. Luo, L. Han, J. Huang, Z. Feng, Z. Chen, J. Xu, B. Peng, Z.L. Wang, Enhanced photocatalytic degradation and H_2/H_2O_2 production performance of S-pCN/$WO_{2.72}$ S-scheme heterojunction with appropriate surface oxygen vacancies, Nano Energy 81 (2021), 105671.

[25] H. Deng, X. Fei, Y. Yang, J. Fan, J. Yu, B. Cheng, L. Zhang, S-scheme heterojunction based on p-type $ZnMn_2O_4$ and n-type ZnO with improved photocatalytic CO_2 reduction activity, Chem. Eng. J. 409 (2021), 127377.

[26] S. Wang, X. Du, C. Yao, Y. Cai, H. Ma, B. Jiang, J. Ma, S-scheme heterojunction/ Schottky junction tandem synergistic effect promotes visible-light-driven catalytic activity, Nano Res. (2022).

[27] S. Ma, D. Yang, Y. Guan, Y. Yang, Y. Zhu, Y. Zhang, J. Wu, L. Sheng, L. Liu, T. Yao, Maximally exploiting active sites on Yolk@shell nanoreactor: Nearly 100% PMS activation efficiency and outstanding performance over full pH range in Fenton-like reaction, Appl. Catal. B: Environ. 316 (2022), 121594.

[28] X. Yang, S. Wang, N. Yang, W. Zhou, P. Wang, K. Jiang, S. Li, H. Song, X. Ding, H. Chen, J. Ye, Oxygen vacancies induced special CO_2 adsorption modes on Bi_2MoO_6 for highly selective conversion to CH_4, Appl. Catal. B: Environ. 259 (2019), 118088.

[29] J. Di, C. Yan, A.D. Handoko, Z.W. Seh, H. Li, Z. Liu, Ultrathin two-dimensional materials for photo- and electrocatalytic hydrogen evolution, Mater. Today 21 (2018) 749–770.

[30] Y. Liu, L. Wang, Q. Yao, X. Gao, X. Du, X. Dou, H. Zhu, X. Yuan, J. Xie, In situ synthesis of bismuth nanoclusters within carbon nano-bundles from metal–organic framework for chloride-driven electrochemical deionization, Adv. Funct. Mater. 32 (2022) 2110087.

[31] F. Zhang, X. Li, Q. Zhao, G. Chen, Q. Zhang, High-performance In_2O_3@PANI core@ shell architectures with ultralong charge carriers lifetime for photocatalytic degradation of gaseous 1,2-dichlorobenzene, Appl. Catal. B: Environ. 263 (2020), 118278.

[32] M. Zhang, C. Xiao, X. Yan, S. Chen, C. Wang, R. Luo, J. Qi, X. Sun, L. Wang, J. Li, Efficient removal of organic pollutants by metal–organic framework derived Co/C yolk–shell nanoreactors: size-exclusion and confinement effect, Environ. Sci. Technol. 54 (2020) 10289–10300.

[33] S. Chen, D. Huang, G. Zeng, W. Xue, L. Lei, P. Xu, R. Deng, J. Li, M. Cheng, In-situ synthesis of facet-dependent BiVO$_4$/Ag$_3$PO$_4$/PANI photocatalyst with enhanced visible-light-induced photocatalytic degradation performance: synergism of interfacial coupling and hole-transfer, Chem. Eng. J. 382 (2020), 122840.

[34] Y. Naciri, A. Hsini, A. Bouziani, K. Tanji, B. El Ibrahimi, M.N. Ghazzal, B. Bakiz, A. Albourine, A. Benlhachemi, J.A. Navío, H. Li, Z-scheme WO$_3$/PANI heterojunctions with enhanced photocatalytic activity under visible light: a depth experimental and DFT studies, Chemosphere 292 (2022) 133468.

[35] X. Zhao, J. Feng, J. Liu, J. Lu, W. Shi, G. Yang, G. Wang, P. Feng, P. Cheng, Metal–organic framework-derived ZnO/ZnS heteronanostructures for efficient visible–light-driven photocatalytic hydrogen production, Adv. Sci. 5 (2018) 1700590.

[36] W. Yu, J. Zhang, T. Peng, New insight into the enhanced photocatalytic activity of N-, C- and S-doped ZnO photocatalysts, Appl. Catal. B: Environ. 181 (2016) 220–227.

[37] Z.-F. Huang, J. Song, X. Wang, L. Pan, K. Li, X. Zhang, L. Wang, J.-J. Zou, Switching charge transfer of $C_3N_4/W_{18}O_{49}$ from type-II to Z-scheme by interfacial band bending for highly efficient photocatalytic hydrogen evolution, Nano Energy 40 (2017) 308–316.

[38] J.W. Thomson, L. Cademartiri, M. MacDonald, S. Petrov, G. Calestani, P. Zhang, G. A. Ozin, Ultrathin Bi_2S_3 nanowires: surface and core structure at the cluster-nanocrystal transition, J. Am. Chem. Soc. 132 (2010) 9058–9068.

[39] Q. Wang, D. Xu, Y. Dong, S. Pang, L. Zhang, G. Zhang, L. Lv, X. Liu, Y. Xia, L. C. Campos, Z. Ren, P. Wang, Unsaturated Nd-Bi dual-metal sites enable efficient NIR light-driven O_2 activation for water purification, Appl. Catal. B: Environ. 319 (2022), 121924.

[40] K.-K. Takashi, M. Masayuki, T. Hideyuki, H. Yoshihiro, N. Taneo, Photoreflectance characterization of built-in potential in MBE-produced As-grown GaAs surface, Proc. SPIE (1990) 56–65.

[41] Y. Shi, L. Li, Z. Xu, X. Qin, Y. Cai, W. Zhang, W. Shi, X. Du, F. Guo, Coupled internal electric field with hydrogen release kinetics for promoted photocatalytic hydrogen production through employing carbon coated transition metal as co-catalyst, J. Colloid Interface Sci. 630 (2023) 274–285.

[42] Q. Chen, X. Chen, Q. Jiang, Z. Zheng, Z. Song, Z. Zhao, Z. Xie, Q. Kuang, Constructing oxide/sulfide in-plane heterojunctions with enlarged internal electric field for efficient CO_2 photoreduction, Appl. Catal. B: Environ. 297 (2021), 120394.

[43] J. Li, L. Cai, J. Shang, Y. Yu, L. Zhang, Giant enhancement of internal electric field boosting bulk charge separation for photocatalysis, Adv. Mater. 28 (2016) 4059–4064.

[44] X. Chen, J. Wang, Y. Chai, Z. Zhang, Y. Zhu, Efficient photocatalytic overall water splitting induced by the giant internal electric field of a g-C_3N_4/rGO/PDIP Z-scheme heterojunction, Adv. Mater. 33 (2021) 2007479.

[45] R.-T. Gao, X. Guo, S. Liu, X. Zhang, X. Liu, Y. Su, L. Wang, Ultrastable and high-performance seawater-based photoelectrolysis system for solar hydrogen generation, Appl. Catal. B: Environ. 304 (2022), 120883.

[46] M. Kan, C. Yang, Q. Wang, Q. Zhang, Y. Yan, K. Liu, A. Guan, G. Zheng, Defect-assisted electron tunneling for photoelectrochemical CO_2 reduction to ethanol at low overpotentials, Adv. Energy Mater. 12 (2022) 2201134.

[47] S. Sun, R. Gao, X. Liu, L. Pan, C. Shi, Z. Jiang, X. Zhang, J.-J. Zou, Engineering interfacial band bending over bismuth vanadate/carbon nitride by work function regulation for efficient solar-driven water splitting, Sci. Bull. 67 (2022) 389–397.

[48] J. Fu, Q. Xu, J. Low, C. Jiang, J. Yu, Ultrathin 2D/2D WO_3/g-C_3N_4 step-scheme H_2-production photocatalyst, Appl. Catal. B: Environ. 243 (2019) 556–565.

[49] A. Wang, J. Ni, W. Wang, X. Wang, D. Liu, Q. Zhu, MOF-derived N-doped ZnO carbon skeleton@hierarchical Bi_2MoO_6 S-scheme heterojunction for photodegradation of SMX: Mechanism, pathways and DFT calculation, J. Hazard. Mater. 426 (2022), 128106.

[50] C. Wu, Z. Xing, B. Fang, Y. Cui, Z. Li, W. Zhou, Polyoxometalate-based yolk@shell dual Z-scheme superstructure tandem heterojunction nanoreactors: encapsulation and confinement effects, J. Mater. Chem. A 10 (2022) 180–191.

[51] J. Miao, Y. Zhu, J. Lang, J. Zhang, S. Cheng, B. Zhou, L. Zhang, P.J.J. Alvarez, M. Long, Spin-state-dependent peroxymonosulfate activation of single-atom M–N moieties via a radical-free pathway, ACS Catal. 11 (2021) 9569–9577.

[52] A. Wang, J. Ni, W. Wang, D. Liu, Q. Zhu, B. Xue, C.-C. Chang, J. Ma, Y. Zhao, MOF Derived Co–Fe nitrogen doped graphite carbon@crosslinked magnetic chitosan Micro–nanoreactor for environmental applications: Synergy enhancement effect of adsorption–PMS activation, Appl. Catal. B: Environ. 319 (2022), 121926.

[53] H. Ma, Y. He, X. Li, J. Sheng, J. Li, F. Dong, Y. Sun, In situ loading of MoO_3 clusters on ultrathin Bi_2MoO_6 nanosheets for synergistically enhanced photocatalytic NO abatement, Appl. Catal. B: Environ. 292 (2021), 120159.

[54] N. Li, R. Li, X. Duan, B. Yan, W. Liu, Z. Cheng, G. Chen, La Hou, S. Wang, Correlation of active sites to generated reactive species and degradation routes of organics in peroxymonosulfate activation by Co-loaded carbon, Environ. Sci. Technol. 55 (2021) 16163–16174.

[55] X. Luo, Y. You, M. Zhong, L. Zhao, Y. Liu, R. Qiu, Z. Huang, Green synthesis of manganese–cobalt–tungsten composite oxides for degradation of doxycycline via efficient activation of peroxymonosulfate, J. Hazard. Mater. 426 (2022), 127803.

[56] D. Li, T. Hua, X. Li, J. Cheng, K. Du, Y. Hu, Y. Chen, In-situ fabrication of ionic liquids/MIL-68(In)–NH_2 photocatalyst for improving visible-light photocatalytic degradation of doxycycline hydrochloride, Chemosphere 292 (2022) 133461.

[57] Z. Zhang, Z. Pan, Y. Guo, P.K. Wong, X. Zhou, R. Bai, In-situ growth of all-solid Z-scheme heterojunction photocatalyst of $Bi_7O_9I_3$/g-C_3N_4 and high efficient degradation of antibiotic under visible light, Appl. Catal. B: Environ. 261 (2020), 118212.